COMPUTERS AND BIOMEDICAL RESEARCH **25,** 218–237 (1992)

# Automated Detection and Classification of Breast Tumors

SHUN LEUNG NG* AND WALTER F. BISCHOF†

**Department of Computing Science and †Department of Psychology, University of Alberta, Edmonton, Alberta, Canada T6G 2E9*

Received March 4, 1991

This paper presents a new method for the mammographic detection and classification of two types of breast tumors, stellate lesions and circumscribed lesions. The method assumes that both types of tumors appear as approximately circular, bright masses with a fuzzy boundary and that stellate lesions are in addition surrounded by a radiating structure of sharp, fine lines. Experimental results for a set of 27 mammograms are presented and the method is shown to have a high detection rate and an extremely low false positive rate. © 1992 Academic Press, Inc.

## I. INTRODUCTION

Breast cancer is one of the leading cancers in the female population. About 25% of all cancers diagnosed in women are breast cancers and about 20% of all lethal cancers are breast cancers (*13*). Treatment of breast cancer is currently effective only if it is detected at an early stage. The most effective method of early detection is mammographic screening (*3*). Implementing such a screening program is, however, difficult since it requires the interpretation of a large volume of breast images by trained radiologists. With recent advances in medical image processing it has become feasible to design automated diagnosis systems, or, on a more modest level, to design systems that can aid radiologists in mammogram interpretation.

Several approaches to analyzing mammograms have been proposed in the past (*1, 6, 8–11, 14*). They can be loosely grouped into three categories. Some approaches use texture measures to either characterize the general appearance of mammograms for breast cancer risk assessment (*11*) or detect regions differing in appearance from the rest of the breast (*6, 8, 10*) to locate suspicious areas. These methods do not, however, use characteristics specific to tumors and thus are limited in their performance. A second category comprises systems that are designed to detect specific types of tumors such as microcalcifications (*4*) or circumscribed masses (*9*). Performance of these systems is generally better because tumor-specific characteristics can be used both for detection of tumors and for elimination of nontumors. Finally, in a third category there are



0010-4809/92 $5.00

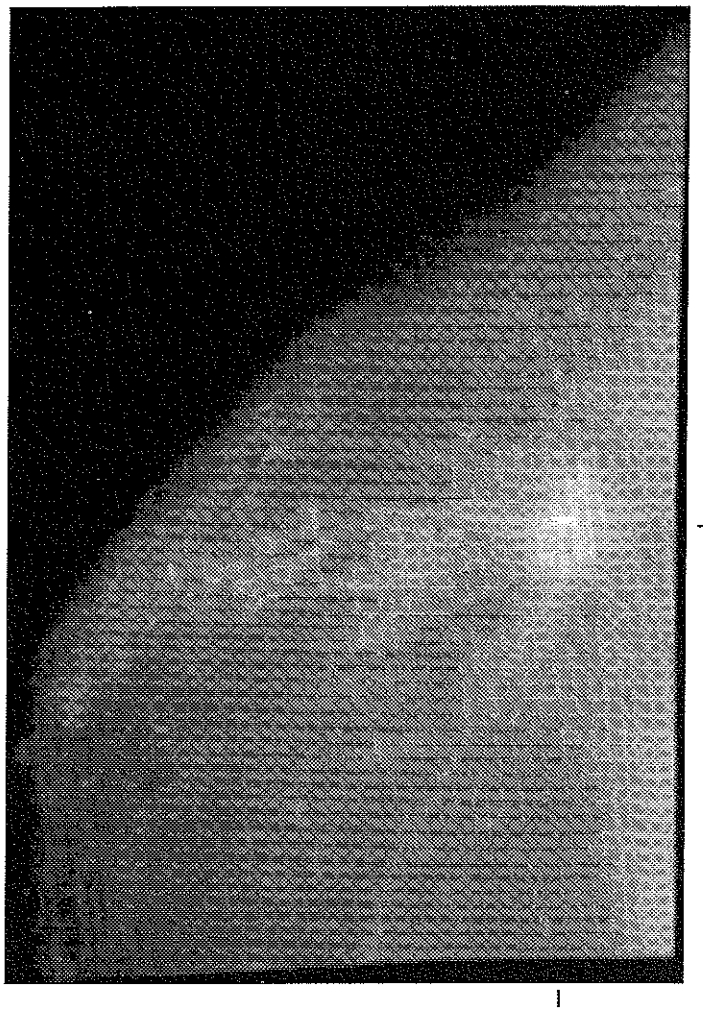

PLATE 1. Mammogram with a stellate lesion. The position of the lesion is indicated by the two lines on the margin.

systems used for differential diagnosis of tumors at *known* tumor locations (*1, 14*). These systems show a very good diagnostic performance, approaching the performance of human experts.

The system described here belongs to the second group and is part of a project with the goal of developing a fully automated breast cancer detection system. The system is designed to detect two types of tumors, stellate lesions and circumscribed lesions, and to perform a differential diagnosis between the two.

Most breast carcinomas have the appearance of stellate lesions (see Plate 1), consisting of a central tumor mass surrounded by a radiating structure of sharp,

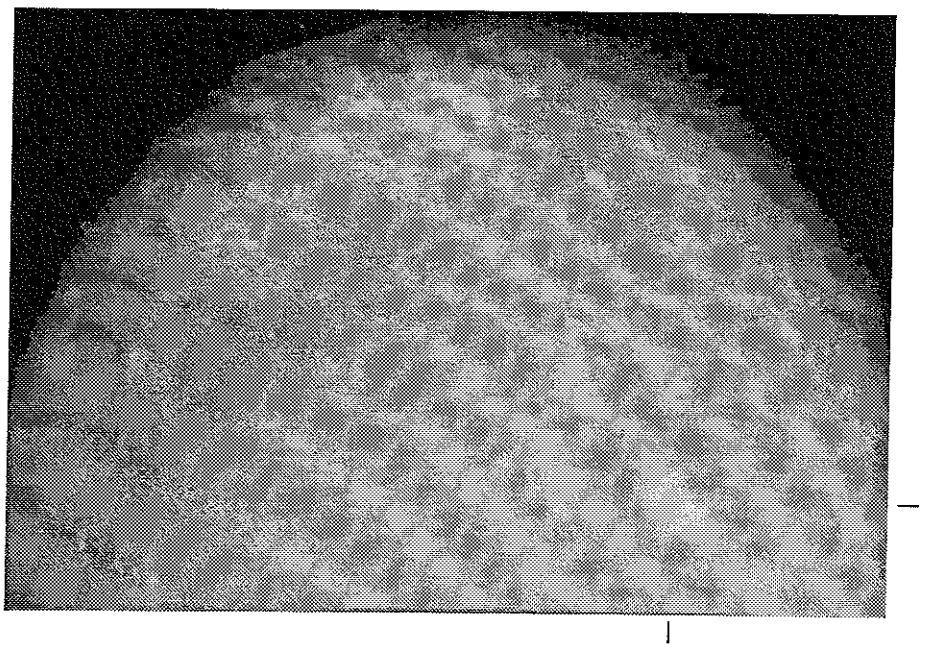

PLATE 2. Mammogram with a circumscribed lesion. The position of the lesion is indicated by the two lines on the margin.

dense, and fine lines, called "spicules," that emanate from the central mass (*15*). The central tumor mass of a malignant stellate lesion is a solid, distinct radiopaque mass and appears as a bright blob in mammograms. Although difficult to perceive when it is small, the central mass is always present. The spicules radiate outward in all directions and vary in length, but generally the average length increases with tumor size. Some stellate lesions are benign in nature and can be differentiated mammographically from malignant lesions with high accuracy. In the present article we concentrate on techniques for detecting only malignant lesions although we believe that similar techniques can be used for detecting benign lesions.

Circumscribed lesions, on the other hand, appear as approximately circular masses (see Plate 2). In malignant lesions the central mass is highly radiopaque and the lesion boundary is fuzzy. Although there are additional signs that can be used for diagnosing circumscribed lesions, brightness, shape, and boundary characteristics are the primary signs and are the only ones used in the present system.

In the work presented here we assume that circumscribed lesions and the central mass of stellate lesions are sufficiently similar in appearance to justify a single detection method. The detection of both lesions can then be decomposed into two subproblems, central mass detection and recognition of the radiating

structure. If there is evidence for the presence of a radiating structure, a lesion is diagnosed as stellate lesion; otherwise it is diagnosed as a circumscribed lesion.

It should be made clear from the outset that the objective of the methods presented here is not to achieve tumor detection with a minimal computational effort. Rather the objective is to achieve the best possible performance in detection and diagnosis of tumors with as much computational effort as is required. In spite of this objective, there are some situations in which the method fails. These cases will be discussed in Section IV.

Below, we first present methods for detecting the radiating structure of stellate tumors (Section II). Then we discuss methods for detecting the central tumor mass and methods for making a differential diagnosis between the two types of lesions (Section III). In the final section we present experimental results and discuss problems and inadequacies of the proposed approach (Section IV).

## II. Radiating Structure Recognition

The radiating structure of stellate tumors is formed by spicules that emanate radially from the central tumor mass. In this section we present three different approaches for detecting this radiating structure. The approaches make different assumptions about the structure of an "ideal" stellate tumor and their performance depends on the extent to which the ideal tumor matches the actual appearance of stellate tumors. The first two approaches are modeled after descriptions provided by expert radiologists and are presented only briefly, while the third and most successful approach, the spine-oriented approach, is presented in full detail. (For a detailed review of all approaches the reader is referred to (*12*).)

1. The *edge-oriented approach* assumes that the spicules of a stellate tumor are narrow and distinctly visible. Lines along the spicule edges should therefore converge to the center of the radial structure.
2. The *field-oriented approach* does not require individual spicules to be distinctly visible, but it assumes that the spicules produce a brightness-gradient field exhibiting a consistent radial structure. Radial lines of this structure should converge in the center of the tumor.
3. The *spine-oriented approach* assumes that the spicules not only are distinctly visible but in addition show a characteristic microstructure. Extracting this microstructure allows finding the center of the radial structure with high accuracy.

The performance of each method is illustrated here with the tumor shown in Plate 1, which is shown magnified and enhanced in Plate 3a.

Before turning to the details of the three proposed approaches we present some aspects common to all methods. First, all mammograms were digitized from film using a camera with resolution 512 × 480 pixels and 256 gray levels. The breast region was automatically extracted from the background and the

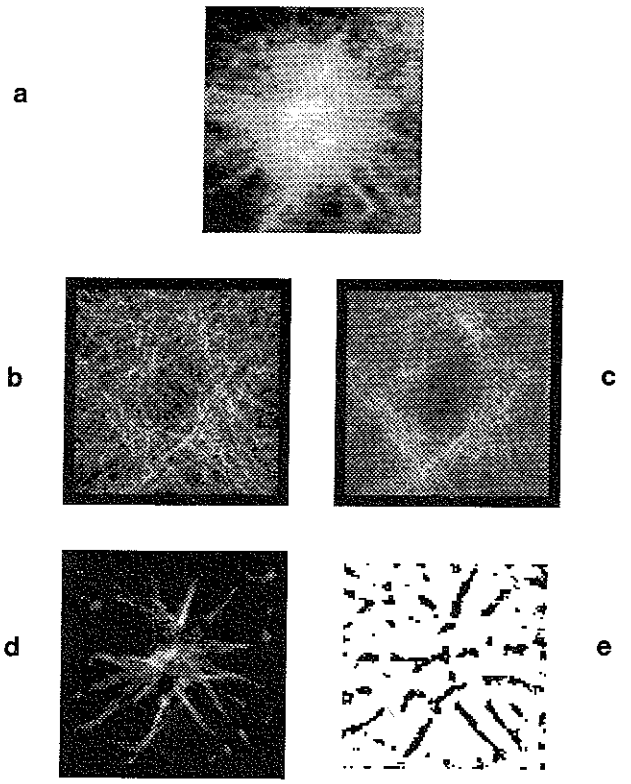


PLATE 3. (a) Enhanced view of the stellate lesion in Plate 1. (b) Response of the edge-oriented approach. (c) Response of the field-oriented approach. (d) Response of the spine-oriented approach. In all three response images bright points correspond to high values of $H(i, j)$ and thus indicate the presence of a radial center at that position. (e) Binary map of all spinal pixels found by the spinal detection method.

gray levels within the breast area were linearly stretched to a full contrast of 256 gray levels. The result of this preprocessing is shown in Plates 1 and 2.

Second, the radial structure recognition methods are all combined with a Gaussian filter to remove high-frequency noise in the digitized mammograms. The Gaussian filter $G$ is defined as

$$G(x, y) = (2\pi\sigma^2)^{-1} \exp[-(x^2 + y^2)/2\sigma^2], \quad [1]$$

where the standard deviation $\sigma$ controls the amount of smoothing. In order to obtain a reasonable amount of noise suppression while at the same time not destroying the very fine spicular structure, a conservative size of $\sigma = 1.5$ pixels was chosen in our implementation. The following notation is used. Let $M(x, y)$ denote the digitized mammogram. The Gaussian-filtered image $I(x, y)$ is then obtained through the convolution $I = M * G$. (Note that this is done for

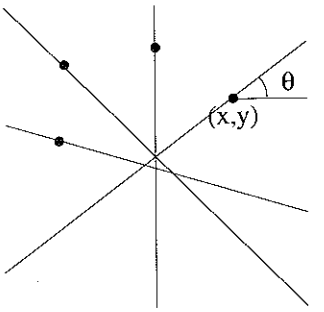


FIG. 1. Sketch illustrating the idea of the Hough transformation. A set of lines defined by radial measurements $(x, y, \theta)$ should converge at a single point or lead to a cluster of intersections near the center of the radial structure.

notational convenience only. The Gaussian operator can be combined with subsequent operators into a single operator.)

Third, all methods use the Hough transformation (*5*) to locate the center of the radial structure. The idea of the Hough transformation is that given a point $(x_k, y_k)$ with radial orientation $\theta_k$( see Fig. 1), the center of the radial structure is constrained to lie on the line defined by the equations

$$\begin{aligned} x &= x_k + r\cos\theta_k \\ y &= y_k + r\sin\theta_k. \end{aligned} \qquad [2]$$

For a set of measurements $(x_k, y_k, \theta_k)$ the center of the radial structure is given by the intersection of all such lines. If there are measurement errors or if the data contain noise, the center of the radial structure is defined by the cluster of intersection points. We now define a two-dimensional histogram $H(i, j)$. For every measurement $(x_k, y_k, \theta_k)$, $H(i, j)$ is increased by one if the line defined by [2] passes through pixel $P(i, j)$, defined by $\{(x, y) : |x - i| < 1/2, |y - i| < 1/2\}$. Peaks or clusters in $H$ then indicate image points that are likely to be at the center of a radial structure.

### *A. Edge-Oriented Method*

The edge-oriented approach is based on the assumption that the radiating structure is formed by a number of very sharp, thin, and radially arranged spicules that are distinctly visible. If a line is drawn passing through an edge point of a spicule and in a direction normal to the edge gradient, it should pass through the center of the radial structure.

To find the center of stellate tumors the following procedure is followed. First all edges in the mammogram are extracted. To reduce noise effects, edge extraction is combined with the Gaussian filter [1] and only edges with a gradient exceeding a certain threshold $T$ are used. All edge pixels $(x_k, y_k)$, with orientation

$\theta_k$ normal to the edge gradient, are then used to find the radial center, using the Hough transformation described above.

In our implementation the spicule edges were detected using the Canny edge detector (*2*) which identifies edge positions with zero-crossings of the second directional derivative in the direction of the principal gradient, i.e.,

$$\frac{\partial^2 I}{\partial \mathbf{n}^2} = 0, \qquad [3]$$

where $\mathbf{n} = \nabla I/|\nabla I|$ is the direction of the principal gradient and $I = M * G$ as before.

The result of the edge-oriented approach for the tumor in Plate 3a is shown in Plate 3b. The discussion of the result is deferred until after the field-oriented approach has been presented, since the results of both approaches are very similar.

### *B. Field-Oriented Method*

The field-oriented approach is based on (*7*). It is similar to the edge-oriented approach but does not assume that the spicules are distinctly visible and thus it does not require that spicule edges be detected. Rather it assumes that the spicules produce a brightness pattern such that the brightness-gradient field follows concentric circles or, equivalently, that the vector field normal to the gradient field has a radial structure. The center of the radial pattern which corresponds to the central tumor mass of the stellate lesion is considered an area free of any regular pattern.

To find the center of stellate tumors the following procedure is followed. First the brightness gradient field

$$\mathbf{g}(x, y) = \left(\frac{\partial I}{\partial x}, \frac{\partial I}{\partial y}\right) \qquad [4]$$

is computed and then the flow field normal to the gradient field is determined. Centers of the radial structures are determined from the flow field measurements $(x_k, y_k, \theta_k)$ using the Hough transformation, as was the case with the edge-oriented approach.

The result of the field-oriented approach for the tumor in Plate 3a is shown in Plate 3c. As can be seen in Plates 3b and 3c, neither the edge-oriented nor the field-oriented approach produces a peak at the center of the stellate tumor. Rather, they produce an annular response. There are two reasons for this. First, both approaches assume that spicules are very narrow, thin lines, in accordance with descriptions found in the literature (e.g., (*15*)). A closer analysis of stellate tumors reveals, however, that the angle subtended by some spicules is obtuse, and this leads to the annular response profile. Thus, the assumptions about the ideal tumor shape of both approaches do not match the actual appearance of stellate lesions. Second, both approaches respond strongly to the boundary of the central tumor mass. In fact, the strongest annular response is produced by

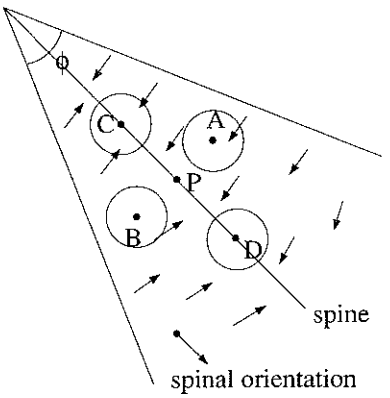


FIG. 2. Ideal microstructure of a spicule. The gradient field on both sides of the spine is indicated by the arrows. In the neighborhood of a spinal pixel $P$ there are two areas (around $A$ and $B$) where the gradient field is coherent and two other areas (around $C$ and $D$) where the gradient field is incoherent. Also shown are the spinal orientation $\mathbf{s}$ and the spicular angle $\phi$.

round objects, such as a white disk, and thus cannot be used as evidence for the presence of a radial structure.

### *C. Spine-Oriented Method*

The spine-oriented method assumes that the spicules are not only distinctly visible but in addition show a characteristic microstructure. In the following we first describe this microstructure and then present the steps required to detect spicules and to detect the center of the radial structure.

Each spicule is assumed to have a specific shape, as shown in Fig. 2. The central line of the spicule is called the *spine* and its orientation, the *spinal orientation*, is defined as pointing toward the dull end of the spicule, i.e., toward the center of the ideal stellate tumor. Pixels on the spine are called *spinal pixels*. Other pixels within a spicule are called *spicular pixels* and their orientation, the *spicular orientation*, is defined as the gradient at that pixel. Within a small local area, spicular pixels point in an almost uniform direction and thus form an oriented field. A closer analysis of the mammograms reveals that the spicular orientation field is oriented mainly in a direction between the direction normal to the spines and the spinal direction, as illustrated in Fig. 2.

Furthermore, the following pattern, called *gradient coherence rule*, can be observed (see Fig. 3). If $P$ is a spinal pixel, then there are two areas (around $A$ and $B$) where the brightness gradient field is coherent, i.e., where the gradient vectors $\mathbf{g}(x, y)$ point to approximately the same direction. There are two other areas (around $C$ and $D$) where the gradient field is incoherent.

In the following, we first describe the method for detecting spicules using the gradient coherence rule, and then the method for locating the center of the radial structure.

*Gradient Coherence Measurement.* Following (7) we define the local coherence of the brightness gradient field $\mathbf{g}(x, y)$ in the neighborhood of $(x, y)$ in the following way. Let $\mathbf{g}(x, y) = [g_x(x, y), g_y(x, y)]$ and $g(x, y) = |\mathbf{g}(x, y)|$, the gradient magnitude. We compute local averages of $g$, $g_x$, and $g_y$ using a Gaussian weighting function $G$; i.e., we compute the convolutions $J(x, y) = G * g$, $J_x(x, y) = G * g_x$, and $J_y(x, y) = G * g_y$. Now we define the local coherence $\chi(x, y)$ of the gradient field at $(x, y)$ as

$$\chi(x, y) = \frac{(J_x^2(x, y) + J_y^2(x, y))^{1/2}}{J(x, y)}. \quad [5]$$

The coherence ranges from zero in the absence of any dominant orientation in the neighborhood of $(x, y)$ to 1 for a highly oriented pattern.

For $\chi(x, y) > 0$ the dominant local orientation is given by $\mathbf{J}(x, y) = [J_x(x, y), J_y(x, y)]$, and the angle $\omega$ of $\mathbf{J}(x, y)$ with the horizontal axis is given by

$$\omega(x, y) = \arctan\left(\frac{J_y(x, y)}{J_x(x, y)}\right). \quad [6]$$

Assume that $P$ is a spinal pixel and that $A$ and $B$ are on the side of the spine as shown in Fig. 2. Let $\mathbf{a} = \mathbf{J}(A)$ and $\mathbf{b} = \mathbf{J}(B)$. The spinal orientation $\mathbf{s}$, pointing toward the dull end of the spicule and thus toward the radial center, can be estimated from $\mathbf{a}$ and $\mathbf{b}$ using

$$\mathbf{s} = \frac{\mathbf{a}}{|\mathbf{a}|} + \frac{\mathbf{b}}{|\mathbf{b}|}. \quad [7]$$

*Gradient Coherence Rule.* The gradient coherence rule, introduced above and illustrated in Fig. 2, states that if $P$ is a spinal pixel then there are two areas $A$ and $B$ in the neighborhood of $P$ where the gradient field is coherent, and two other areas $C$ and $D$ where it is incoherent.

To establish whether pixel $P$ is a spinal pixel, a small area centered at $P$ is divided into four quadrants $Q_1$–$Q_4$, and four pixels $A$, $B$, $C$, and $D$ are chosen in each quadrant at a fixed distance from $P$ (see Fig. 3a). If gradient coherence in the neighborhood of $P$ is low, i.e., if both measures $\chi(A)\chi(B)$ and $\chi(C)\chi(D)$ are low (less than 0.8 in our implementation), $P$ is rejected as a spinal pixel. Otherwise we can tell which pair of quadrants the (potential) spine falls on by comparing $\chi(A)\chi(B)$ with $\chi(C)\chi(D)$.

In addition, we have to test whether the gradient field in the neighborhood of $P$ shows the characteristic structure illustrated in Fig. 2. The interested reader is referred to the Appendix for a detailed description of the tests. Here it suffices to say that the gradients at $A$ and $B$ have to point more or less toward $P$, and that these tests have to work for arbitrary spinal orientations. If a pixel $P$ has passed all tests it is considered a spinal pixel. The spinal pixels for the tumor shown in Plate 3a are shown in Plate 3e.

*Estimation of Spinal Parameters.* Each spinal pixel is described by three parameters which capture the essential information about a spicule:

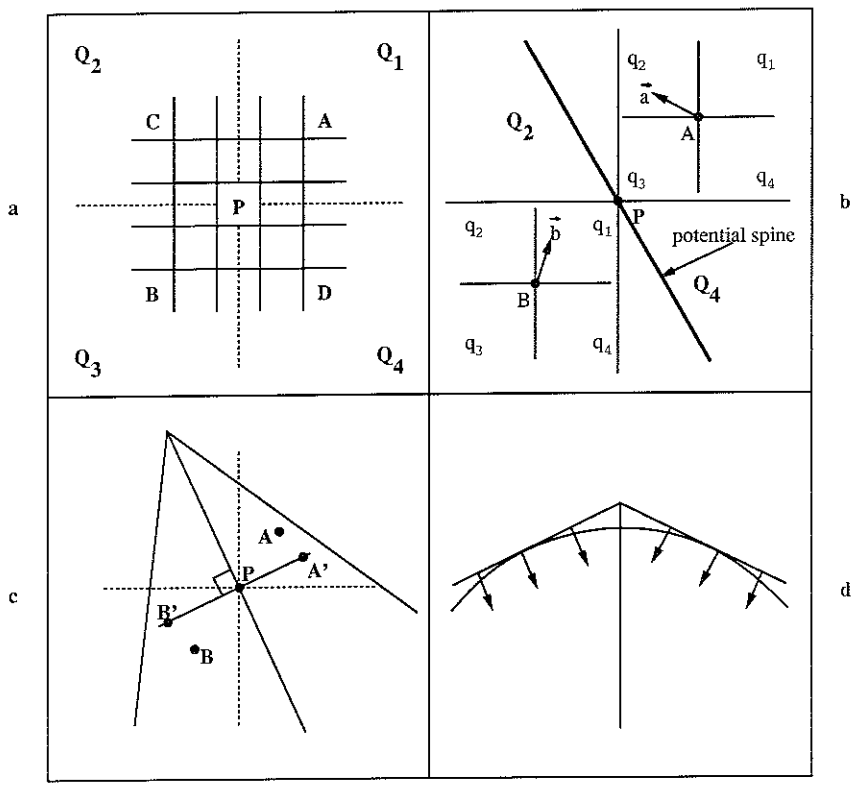


FIG. 3. Four situations illustrating the detection of a spinal pixel. (a) The gradient field is measured at pixels $A$, $B$, $C$, and $D$ in quadrants $Q_1$–$Q_4$ in the neighborhood of a spinal pixel $P$. (b) Vectors **a** and **b** denote the averaged gradient fields at pixels $A$ and $B$. Also shown are the four quadrants $q_1$–$q_4$ and the orientation $\omega$ of the gradient field at pixels $A$ and $B$. (c) Improved estimates of the spinal orientation **s** are obtained from gradient measurements at points $A'$ and $B'$. The two points lie on a line normal to the initial estimate of **s** and at a distance of $\overline{AP}$ from $P$. Subpixel accuracy is obtained through bilinear interpolation. (d) Pixels on the boundary of large objects may pass the spinal consistency tests but are rejected as spinal pixels if the spicular angle $\phi$ is too large.

1. The *location* is given by the pixel position.
2. The *spinal orientation* is given by the estimate **s**.
3. The *spicular angle* $\phi$ defines the acuteness of a spicule. It is estimated from **a** and **b** using

$$\phi = \pi - \arcsin\left(\frac{|\mathbf{a} \times \mathbf{b}|}{|\mathbf{a}||\mathbf{b}|}\right). \qquad [8]$$

Information about the spicular angle is used in the following way. Very obtuse spicular angles indicate that the spinal pixel detection is responding to the boundary of a central tumor mass or of some other large object, as illustrated

in Fig. 3d. Thus if the spicular angle exceeds a threshold $T_\phi$ (130° in our implementation), $P$ is rejected as a spinal pixel.

*Detection of Radial Center.* Once all spinal pixels have been detected and their parameters estimated, the radial centers are located using the Hough transformation, as was the case with the edge-oriented and the field-oriented approaches. However, the spine-oriented approach provides a tighter constraint on the position of the radial center. Given a spinal position $P$ and a spinal orientation vector $\mathbf{s}$, the position of the radial center is constrained to lie on the line $P + \gamma\mathbf{s}$, $\gamma > 0$. The other two approaches provide a nondirected estimate only. Furthermore, given that the position constraint is a semi-infinite line, an additional constraint can be used. As was described previously, the central mass of a stellate tumor is brighter than the background. Therefore, brightness along the line from a spinal pixel $P$ in the direction of the spinal orientation $\mathbf{s}$ should increase, reach a local maximum at the tumor center, and then decrease. The endpoint of the radial line can be set at the point where brightness drops a fixed amount (two gray levels in our implementation) below the current maximum along $\mathbf{s}$. Let this point be at $P + c\mathbf{s}$. Then the radial center is constrained to lie on the finite line defined by

$$P + \gamma\mathbf{s}, \qquad 0 \leq \gamma \leq c. \tag{9}$$

We can now compare the results of the edge-oriented approach (Plate 3a), of the field-oriented approach (Plate 3b), and of the spine-oriented approach (Plate 3d). The first two approaches produce annular responses instead of peaks for two reasons: first, estimated spicular angles are often obtuse and, second, both approaches respond not only to spicules but also to the boundary of the central tumor mass. The spine-oriented approach is more robust for several reasons. First, its response is unaffected by obtuse spicular angles. Second, it provides a more accurate estimate of the true radial direction. Third, it provides a tighter constraint on the position of the radial center as given in [9].

*Spicule Removal.* The spine-oriented approach has one further advantage. In the next section we present a method for detecting the central, bright tumor mass of stellate tumors and of circumscribed masses. That method responds best to a perfectly circular bright area, e.g., a white disk superimposed on a darker background. Its response is weakened to the extent that the actual appearance of a tumor deviates from this ideal shape. In the case of stellate tumors, its response is thus weakened by the presence of the spicular structure. The spine-oriented approach provides accurate information about the presence, position, and orientation of spicules and thus enables us to remove them before the central mass detection process is applied.

Spicule removal is achieved through application of a spicule-smearing filter. The spicule-smearing filter is applied at the position of a spinal pixel $P$ at an orientation normal to the spinal orientation, as illustrated in Fig. 4a. Ideally, the gray-level values of the area inside the spicule should be replaced by the gray-level value of the surrounding background. This is approximately achieved using a directional selective median filter whose kernel is shown in Fig. 4b.

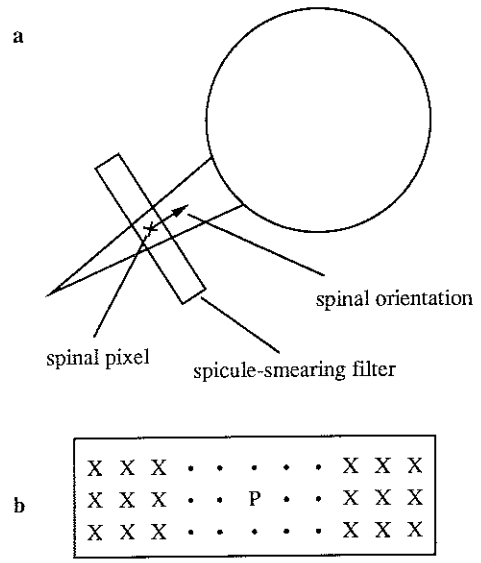


FIG. 4. (a) Situation illustrating the application of the spicule-smearing filter. The filter is applied at a spinal pixel and is oriented normal to the spinal orientation. (b) Shape of the spicule-smearing filter with center at pixel $P$. Pixels marked "X" are used to obtain an estimate of the background gray level.

When this filter is applied to a spinal pixel $P$ the gray level of $P$ is replaced by the median of the gray levels at the pixel positions marked $X$, provided that the new gray level is darker than the old gray level. This is because the intensity of spinal pixels is normally higher than that of nearby background pixels.

The steps required for radial structure recognition using the spine-oriented approach can be summarized as follows. First, all spinal pixels are located in the whole breast area using the method described in Section C. The outcome of this stage is a map of all spinal pixels together with their associated descriptors, spinal orientation, and spicular angle. Binary maps of all spinal pixels for the two lesions in Plates 1 and 2 are shown in Figs. 5 and 6. As a final step in this stage, the spicule-smearing filter is applied to the original image.

## III. Central Mass Detection

As discussed in the Introduction, stellate lesions can be described as being composed of two major components: a radial structure of spicules and a bright central tumor mass. The appearance of circumscribed lesions can be described as a bright, approximately circular area with a fuzzy boundary, superimposed on a darker background. After the spicules of stellate tumors have been removed, as described in the previous section, the appearances of both types of tumors are similar. This allows us to use the same method to detect both circumscribed lesions and the central mass of stellate lesions.

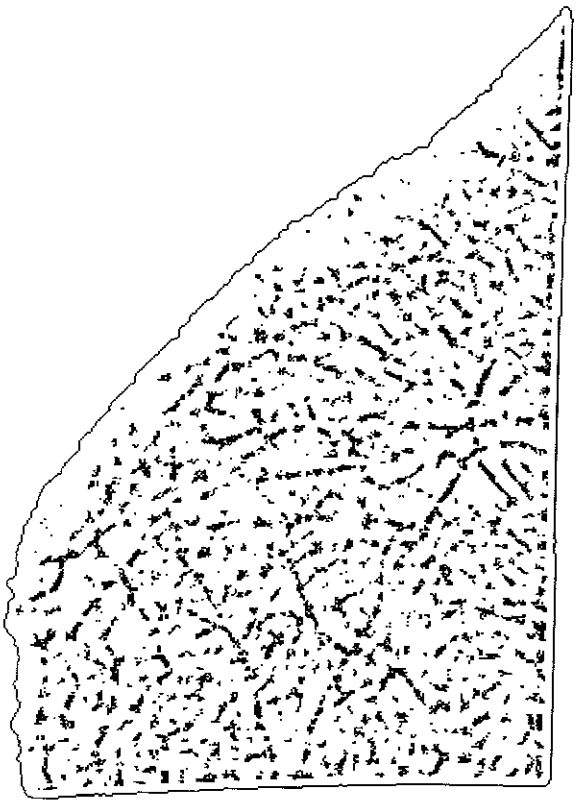

FIG. 5. Binary map of all spinal pixels found for the mammogram in Plate 1.

### *A. Detection*

There are two main approaches to the detection of tumor masses: *segmentation* and *template matching*. In the segmentation approach, one first detects all image regions that are brighter than adjacent areas and then determines whether the shape of the detected regions is approximately circular, e.g., whether it is elliptical with a low eccentricity value. In our work we have the alternative approach, namely template matching. Details of this approach have been described elsewhere (*9*) and we present only a brief summary here.

Templates such as the one shown in Fig. 7 are used to detect the central mass. Likely positions of central masses are given by positive peaks in the (normalized) cross-correlation of this template and the mammogram image. The strongest response is produced by a circular bright region superimposed on a dark background, with the region diameter matching the diameter of the central region of 1s in the template. The ring of 0s in the template allows the image region to deviate slightly from a perfectly circular shape without affecting the magnitude of the cross-correlation peak.

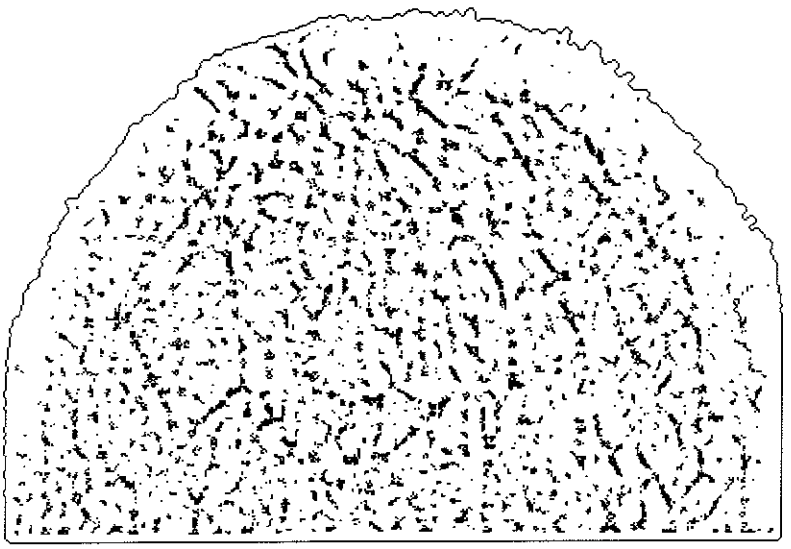

FIG. 6. Binary map of all spinal pixels found for the mammogram in Plate 2.

Since the diameters of central tumor masses vary over a large range, we use a set of templates with different diameters of central region, ranging from 12 to 56 pixels in our implementation. The diameter of the template producing the strongest cross-correlation peak is then taken as an estimate of the diameter of the tumor mass.

Given a template $T$, such as that in Fig. 7, with the origin (0, 0) at the center, and a mammogram image $M$, the normalized cross-correlation $R(x, y)$ is defined as

$$R(x, y) = \frac{\sum_{(i,j)\in D} t(i, j)m(x + i, y + j)}{(\sum_{(i,j)\in D} t^2(i, j) \sum_{(i,j)\in D} m^2(x + i, y + j))^{1/2}}, \qquad [10]$$

where

| | | | | | | | | |
|---|---|---|---|---|---|---|---|---|
| | | -1 | -1 | -1 | | | | |
| | -1 | -1 | 0 | -1 | -1 | | | |
| -1 | -1 | 0 | 1 | 0 | -1 | -1 | | |
| -1 | -1 | 0 | 1 | 1 | 1 | 0 | -1 | -1 |
| -1 | 0 | 1 | 1 | 1 | 1 | 1 | 0 | -1 |
| -1 | -1 | 0 | 1 | 1 | 1 | 0 | -1 | -1 |
| -1 | -1 | 0 | 1 | 0 | -1 | -1 | | |
| | -1 | -1 | 0 | -1 | -1 | | | |
| | | -1 | -1 | -1 | | | | |

FIG. 7. Central mass template for a central region diameter of 5 pixels.

$$t(i,j) = T(i,j) - \frac{1}{N}\sum_{(i,j)\in D} T(i,j)$$
$$m(i,j) = M(i,j) - \frac{1}{N}\sum_{(i,j)\in D} M(i,j) \qquad [11]$$

and where $D$ is the set of template pixels and $N$ is the number of nonzero template pixels. Note that [10] gives a definition of normalized cross-correlation and that more efficient forms can be used in an implementation. Local maxima of the cross-correlation function $R$ correspond to possible positions of central tumor-masses.

The potentially large set of tumor positions given by the positions of cross-correlation peaks is reduced using the following set of criteria. First, local maxima with a correlation value $R < 0.2$ are discarded. This includes negative peaks that would correspond to dark regions on a bright background. Second, local maxima that are spatially very close are taken as resulting from a single image phenomenon, for example, as resulting from a single tumor. Clusters of local peaks are therefore combined into a single potential tumor site. Third, a percentile method is used to reduce the number of potential tumor sites; i.e., only a fixed percentage (2.5% in our implementation) of the strongest peaks are further analyzed as potential tumors. This eliminates the problem, for mammograms with rich textures, of a large number of potential tumor sites being generated.

### *B. False Positive Removal*

The percentile method produces a fixed number of potential tumor locations, independent of the true number of tumors in a mammogram, including the case in which there is no tumor present. Two techniques, described in detail in (*9*) are used to remove false positives (often also referred to as "false alarms").

The *histogram test* is based on the assumption that there is a significant contrast between a tumor area and the surrounding background. A gray-level histogram of a region containing both tumor region and background should therefore be bimodal (or possibly multimodal). If the histogram at a given position is unimodal or flat, it is unlikely that this position corresponds to the center of a tumor mass. The region in which the histogram is computed must be large enough to include some of the background area to ensure bimodality. An estimate of the tumor mass diameter is obtained from the template with the maximum cross-correlation value; the histogram can then be computed over a circular area with a larger diameter.

The *neighborhood test* is based on the following observation. Due to the fuzzy boundary of tumor masses, the peaks in the cross-correlation $R$ are relatively flat at tumor positions but are usually sharp at nontumor positions. Thus, if the cross-correlation drops rapidly in the neighborhood of a peak, the position is rejected as a potential tumor site.

Experimental results reported in (*9*) show that these two false positive tests

are very effective in removing nontumors from the list of potential tumors, leaving on the average only about 1.7 nontumors per mammogram. What remains to be done is to decide whether the tumors detected are circumscribed lesions or stellate lesions.

### *C. Tumor Differentiation*

The principle underlying the differential diagnosis between circumscribed lesions and stellate lesions is very simple. If a lesion is at the center of a radial spicular structure it is diagnosed as a stellate lesion; otherwise, it is diagnosed as a circumscribed lesion. We define the spicularity of a lesion as the number of spinal pixels connected to a lesion. A spinal pixel is considered connected to a lesion if it satisfies the following two conditions. (1) The spinal pixel is not located inside any central mass. (2) The spinal direction line defined in [9] crosses the boundary of the central mass.

As the diameter of a tumor increases, there is an increasing probability that the central mass touches some scattered spinal pixels. Furthermore, large stellate lesions tend to have longer spicules, as was discussed in the Introduction. Therefore, the spicularity measure of lesions should be normalized by the diameter, and it is defined as the ratio of the number of connected spinal pixels to the diameter of the lesion. Now we can formulate a decision rule. If the spicularity of a lesion exceeds a criterion value $c$ ($c = 7$ in our implementation) it is diagnosed as a stellate tumor; otherwise it is diagnosed as a circumscribed tumor.

The two lesions in Plates 1 and 2 are shown again in Plates 4 and 5, with a circle around the central mass and all spinal pixels connected to the central mass. Both the stellate lesion (Plates 1 and 4) and the circumscribed lesion (Plates 2 and 5) are diagnosed correctly.

## IV. Results and Discussion

The method presented in this paper was developed using a small training set of mammograms. Parameters related to the radial structure recognition were determined from this training set. Parameters related to central mass detection were taken from (9). The method was then evaluated using a set of 27 mammograms, containing 23 stellate lesions and 4 circumscribed lesions.

In comparing the diagnoses produced by the computer and by the radiologist we cannot expect that the tumor areas found are exactly the same. Therefore, the following criterion was adopted. The radiologist drew a circle around the central mass of stellate tumors and around circumscribed lesions. If the intersection of this circle and the nearest area indicated by the computer overlapped by more than 50%, the tumor was considered detected; otherwise it was considered missed.

Of the 27 lesions, 22 were detected by the computer and 5 were missed; i.e., the hit rate was 81%. Of the 22 detected lesions 2 were misclassified. One stellate lesion was diagnosed as a circumscribed, and one circumscribed lesion

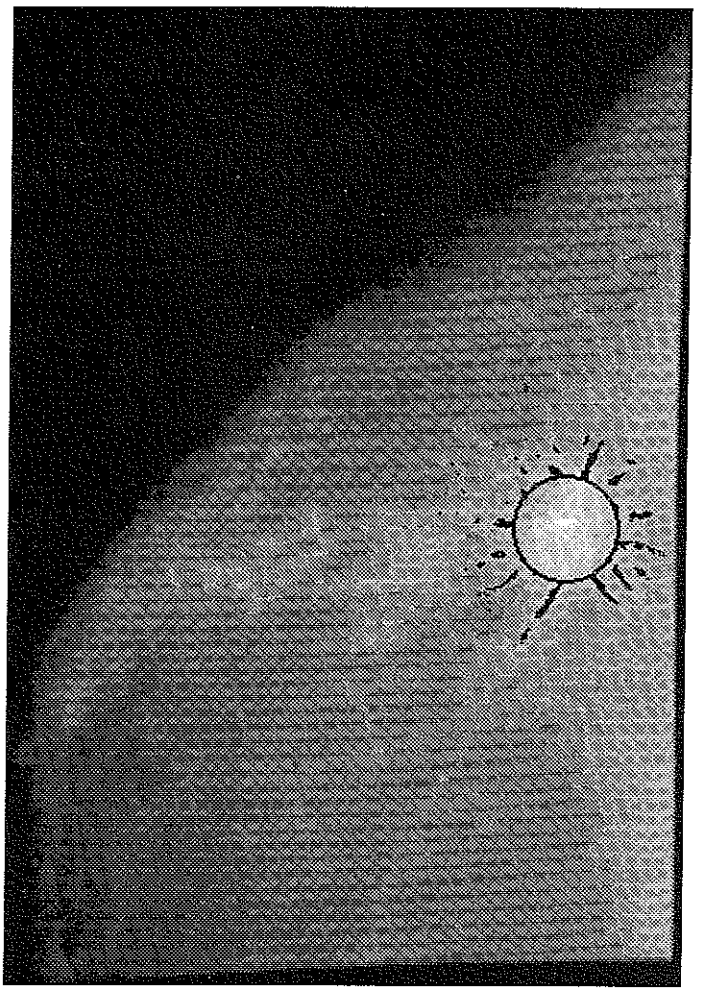

PLATE 4. Final result of the proposed approach for the stellate lesion in Plate 1. The circle indicates position and size of the central mass as found by the central mass detection method. All spinal pixels that are not connected to the central mass have been removed. The lesion is classified as stellate since the spicularity value is high.

was diagnosed as stellate. In addition, a total of 6 lesions were indicated by the computer at positions where the radiologist did not indicate any suspicious area; i.e., there were, on the average, 0.2 false positive per mammogram. Although the detection rate is less than perfect, we judge the performance of the proposed method as very good because, on the other hand, the false positive rate is extremely low compared to other published methods. (Hand (*6*), for example, reports an average of over 50 false positives per mammogram.)

Of the five missed lesions, three were partially obscured by other anatomical

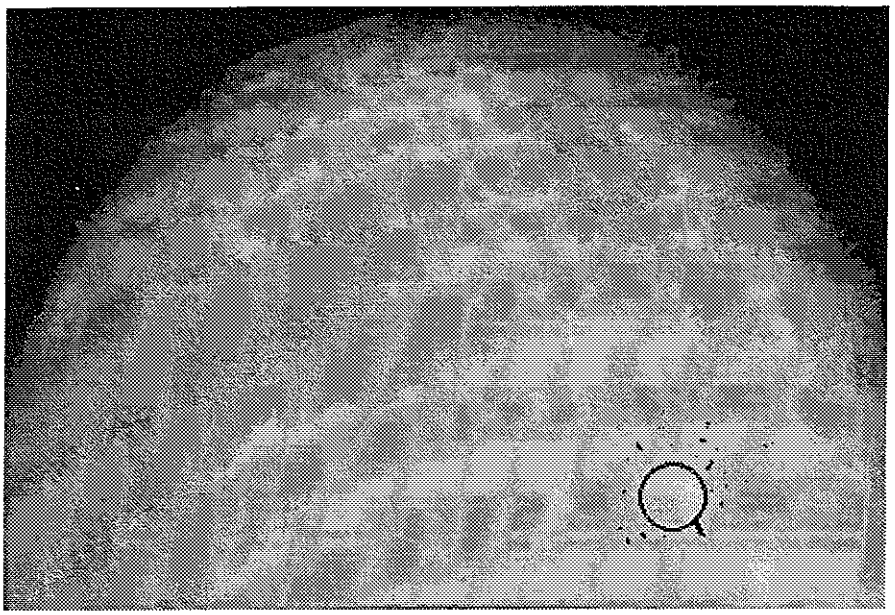

PLATE 5. Final result of the proposed approach for the circumscribed lesion in Plate 2. The circle indicates position and size of the circumscribed mass as found by the central mass detection method. A few spinal pixels connected to the mass are found. However, the lesion is classified as circumscribed since the spicularity value is low.

structures (breast parenchyma). In the other two cases the central tumor mass was too diffuse to be detected by the central mass detector. Both situations are similar in the sense that there is only partial evidence in the image for the presence of a lesion. Detection in such situations is feasible only if evidence from partial clues is very strong. The map of spinal pixels (Fig. 6) indicates that the spinal pixel detection method, in spite of its complexity, does not respond specifically enough to spicules, but responds to a variety of image patterns. Hence, evidence for a radiating structure alone cannot be used for detecting stellate lesions. Similarly, the criteria for detecting the central mass of stellate tumors and circumscribed masses have to be chosen very conservatively. Otherwise, too many false positives would be generated in a typical mammogram. This clearly indicates that further significant progress in computer-based detection of breast cancers depends on the development of methods that respond very specifically to the characteristics of a tumor, with whatever computational effort that may be required.

## APPENDIX

Outlined below are the detailed tests for verifying that the gradient field in the neighborhood of a spinal pixel $P$ is in accordance with the structure illustrated in Fig. 2.

If $P$ is a spinal pixel, a small area centered at $P$ is divided into four quadrants $Q_1$–$Q_4$, and four pixels $A$, $B$, $C$, and $D$ are chosen in each quadrant at a fixed distance from $P$ (see Fig. 3a). If gradient coherence in the neighborhood of $P$ is low, i.e., if both measures $\chi(A)\chi(B)$ and $\chi(C)\chi(D)$ are low, $P$ is rejected as a spinal pixel. Otherwise we can tell which pair of quadrants the (potential) spine falls on by comparing $\chi(A)\chi(B)$ with $\chi(C)\chi(D)$.

Without loss of generality, assume $\chi(A)\chi(B) > \chi(C)\chi(D)$; i.e., the spine is assumed to fall on quadrants $Q_2$ and $Q_4$ (see Fig. 3b). Using a set of consistency rules we now determine whether $P$ is indeed a spinal pixel. A small area centered at pixels $A$ and $B$ is divided into four quadrants $q_1$–$q_4$. Let $\mathbf{a}$ and $\mathbf{b}$ denote the averaged gradient vectors at $A$ and $B$, respectively, i.e., $\mathbf{a} = \mathbf{J}(A)$ and $\mathbf{b} = \mathbf{J}(B)$, and let $\omega_a$ and $\omega_b$ denote the angle of the two vectors with the horizontal axis. Furthermore, let $\mathbf{a} \in q_i$ denote "vector $\mathbf{a}$ points to quadrant $q_i$." $P$ is rejected as a spinal pixel if any of the following conditions holds:

(i) $\mathbf{a} \in q_1$
(ii) $\mathbf{b} \in q_3$
(iii) $\mathbf{a} \in q_2$ and $\mathbf{b} \in q_2$ and $\omega_a < \omega_b$
(iv) $\mathbf{a} \in q_4$ and $\mathbf{b} \in q_4$ and $\omega_a > \omega_b$
(v) $\mathbf{a} \in q_2$ and $\mathbf{b} \in q_4$
(vi) $\mathbf{a} \in q_4$ and $\mathbf{b} \in q_2$.

In conditions (i) to (iv) one or both of the gradients points away from the spine. In conditions (v) and (vi) both gradients are approximately parallel, pointing into opposite directions.

The next set of conditions is tested only if the spinal orientation $\mathbf{s}$, as defined in [7], is neither nearly vertical nor nearly horizontal (to within 10° in our implementation). In this case $P$ is rejected as a spinal pixel if any of the following conditions holds:

(vii) $\mathbf{a} \in q_3$, $\mathbf{b} \in q_2$, and $\mathbf{s} \in q_3$
(viii) $\mathbf{a} \in q_3$, $\mathbf{b} \in q_4$, and $\mathbf{s} \in q_3$
(ix) $\mathbf{a} \in q_2$, $\mathbf{b} \in q_1$, and $\mathbf{s} \in q_1$
(x) $\mathbf{a} \in q_4$, $\mathbf{b} \in q_1$, and $\mathbf{s} \in q_1$.

In all four conditions (vii) to (x) the orientation of $\mathbf{s}$ contradicts the assumption that the spine falls on quadrants $Q_2$ and $Q_4$.

Finally, to obtain more accurate estimates of the spinal orientation $\mathbf{s}$ two new positions $A'$ and $B'$ are determined on a line normal to $\mathbf{s}$ and at the same distance as $\overline{PA}$ and $\overline{PB}$ (see Fig. 3c). The new estimate of the spinal orientation $\mathbf{s}'$ is given by

$$\mathbf{s}' = \mathbf{a}'/|\mathbf{a}'| + \mathbf{b}'/|\mathbf{b}'|,$$

where $\mathbf{a}' = \mathbf{J}(A')$ and $\mathbf{b}' = \mathbf{J}(B')$. If the estimates $\mathbf{s}$ and $\mathbf{s}'$ differ by more than a preset amount (15° in our implementation) pixel $P$ is rejected as a spinal pixel, since large differences in the estimates indicate that the gradient field in the neighborhood of $P$ does not exhibit the required consistency.

## ACKNOWLEDGMENTS

This work was supported by the Canadian Natural Sciences and Engineering Council under Grants OGP38521 and EQP42012. We thank Dr. Castor from the Cross Cancer Institute for all his help. We thank Vince Di Lollo and an anonymous reviewer for helpful comments.

## REFERENCES

1. ACKERMAN, L. V., AND GOSE, E. E. Breast lesion classification by computer and xeroradiograph. *Cancer* **30,** 1025 (1972).
2. CANNY, J. A variational approach to edge detection. *In* "Proceedings, National Conference on Artificial Intelligence, August 1983," pp. 22–26.
3. CASELDINE, J., BLAMEY, R., ROEBUCK, E., AND ELSTON, C. "Breast Disease for Radiographers." Wright, Toronto, 1988.
4. CHAN, H.-P., DOI, K., GALHOTRA, S., VYVORNY, C. J., MACMAHON, H., AND JOKICH, P. M. Image feature analysis and computer-aided diagnosis in digital radiography. i. Automated detection of microcalcifications in mammography. *Med. Phys.* **14,** 538 (1987).
5. DUDA, R. O., AND HART, P. E. "Pattern Classification and Scene Analysis." Wiley, New York, 1973.
6. HAND, W., SEMMLOW, J. L., ACKERMAN, L. V., AND ALCORN, F. S. Computer screening of xeromammograms: A technique for defining suspicious areas of the breast. *Comput. Biomed. Res.* **12,** 445 (1979).
7. KASS, M., AND WITKIN, A. Analyzing oriented patterns. *Comp. Vision Graphics Image Processing* **37,** 362 (1987).
8. KIMME, C., O'LOUGHLIN, B. J., AND SKLANSKY, J. Automatic detection of suspicious abnormalities in breast radiographs. *In* "Data Structure, Computer Graphics and Pattern Recognition," (A. Klinger, K. Fu, and T. Kunii, Eds.), pp. 427–447. Academic Press, New York, 1975.
9. LAI, S. M., LI, X., AND BISCHOF, W. F. On techniques for detecting circumscribed masses in mammograms. *IEEE Trans. Med. Imaging* **8,** 377 (1989).
10. LAU, T.-K. In search of breast carcinoma: A mammographic asymmetry approach. Master's thesis, The University of Alberta, 1990.
11. MAGNIN, I. E., CLUZEAU, F., AND ODET, C. L. Mammographic texture analysis: An evaluation of risk for developing breast cancer. *Opt. Eng.* **25**(6), 780 (1986).
12. NG, S. L. Breast cancer diagnosis by computer. Master's thesis, The University of Alberta, 1990.
13. SADOWSKY, N., AND KOPANS, D. B. Breast cancer. *Radiol. Clin. North Am.* **21**(1), 51 (1983).
14. SMITH, K. T., WAGNER, S. L., GUENTHER, R. B., AND SOLMON, D. C. The diagnosis of breast cancer in mammograms by the evaluation of density patterns. *Radiology* **125,** 383 (1977).
15. TABÁR, L., AND DEAN, P. B. "Teaching Atlas of Mammography," 2nd ed. Georg Thieme, Stuttgart, 1985.